Northward Pathway Across the Tropical North Pacific Ocean Revealed by Surface Salinity: How do El Niño Anomalies Reach Hawaii?

Audrey Hasson, Martin Puy, Jacqueline Boutin, Éric Guilyardi, Rosemary Morrow

Northward Pathway across the Tropical North Pacific Ocean Revealed by Surface Salinity: How do El Niño Anomalies Reach Hawaii?

Audrey Hasson[1], Martin Puy[2], Jacqueline Boutin[1], Eric Guilyardi[1], Rosemary Morrow[3]

[1] *LOCEAN, UMR 7159, CNRS, UPMC, IRD, MNHN, Paris, France*

[2] *UTIG, Austin, Texas*

[3] *LEGOS, UMR 5566, CNES, CNRS, IRD, UPS Toulouse III, Toulouse, France*

Submitted to Journal of Geophysical Research: Oceans on the mm/dd/yyyy

Abstract (236 words)

Using the unprecedented 7-year monitoring of sea surface salinity (SSS) from the Soil Moisture Ocean Salinity (SMOS) satellite mission, an unexpected large-scale anomaly at 20ºN is studied in the tropical Pacific Ocean following the 2015-2016 extreme El Niño event. This basin-wide negative anomaly (below -0.3) is present in October 2015 between 15 and 25ºN, reaching the Hawaiian archipelago. It has not been previously observed during El Niño events. It is accompanied by a negative equatorial SSS anomaly at the dateline (below -0.5) which has been previously described as an El Niño-associated SSS anomaly. A wide range of observations (in situ and space-borne) and a state-of-the-art ocean model simulation are used together to characterize and understand the mechanisms leading to this singular SSS signal. The extra-equatorial negative SSS anomaly is found to be a superposition of a persisting SSS anomaly due to the 2014 weak El Niño and of the larger 2015-2016 El Niño SSS anomaly. Both were advected northward in the tropical current system by the mean Ekman currents and hypothetically by instabilities in the zonal currents patterns. An analysis of analogous structures in the past 20 years shows that this northward displacement of SSS anomalies is not El Niño specific, even if their advection is enhanced during El Niño events. This study shows that when surface freshwater fluxes are weak SSS, unlike sea surface temperature, can be used to trace water mass displacement for up to 20 months.

1. Introduction

The tropical Pacific Ocean is characterized by a large band of low sea surface salinity (SSS) centered around 10ºN, with freshpools on each side of the Pacific Ocean: The West-Pacific fresh-pool (WPFP) (Delcroix and Picaut, 1998) and East-Pacific fresh-pool (EPFP) (Alory et al. 2012) respectively (Fig. 1a). Higher salinities on the poleward sides of the low SSS band belong to the sub-tropical salinity maximums described by Hasson et al. (2013a) and Gordon et al. (2015). If the mean SSS field is mainly due to the surface freshwater fluxes, as indicated by its agreement with the 0 and -1.5 $m.yr^{-1}$ isohyets (Fig. 1a), the meridional shift between the two structures reveals the importance of ocean dynamics (Yu et al. 2011, Hasson et al., 2013b, Tchilibou et al. 2015, Sena-Martins and Stammer, 2015). The spatial distribution of

the tropical Pacific SSS is characterized by longitudinal gradients along the Equator and 20ºN with strong seasonal and interannual variations in their amplitude and zonal location (Fig. 2ac, Maes et al., 2014, Kao and Lagerloef, 2014). At the Equator, the mean seasonal cycle consists of an extension and intensification of the WPFP towards the east in the second half of the year and an extension of the EPFP to the west from November to June each year. At 20ºN, the low SSS zonal variations are synchronous with the equatorial WPFP in the west. In the east, they are shifted with respect to the equatorial EPFP cycle by a few months: their extending phase occurs between June and January. This is consistent with the latitudinal displacement of the seasonal SSS anomaly (SSSA) associated with the Intertropical Pacific Convergence Zone (ITCZ) seasonality (Yu et al. 2015 and Sena-Martins and Stammer, 2015). Figure 2 also shows large year-to-year variations, following the El Niño Southern Oscillation (ENSO) phase, the leading mode of interannual variability in the Tropical Pacific. ENSO has both local and global impacts on the oceanic and atmospheric circulations and leads to many environmental impacts and societal havoc (Wang and Picaut 2004, McPhaden et al. 2006 and Sarachik and Cane, 2010). It includes a warm phase, El Niño, and a cold phase, La Niña (see Philander, 1989) which intensity are usually measured by the Niño 3.4 index (surface temperature anomaly within the 3.4 region – 5ºS-5ºN, 170º-120ºW) shown on Figure 2. The relationship between ENSO and the sea surface temperature (SST) is well described in the literature. At the equator, ENSO is associated with the zonal displacement of the western Pacific warm pool (WPWP, Fig. 2bd). The WPWP plays a key role in the zonal basin-scale atmospheric circulation called the Walker Circulation which is greatly perturbed during ENSO events.

A number of studies have explored the connection between salinity and ENSO (e.g. Delcroix and Picaut, 1998, Picaut et al., 2001, Gouriou and Delcroix, 2002, Bosc et al. 2009, Qu et al., 2014, Qu and Yu, 2014). Deep atmospheric convection, associated with the ascending branch of the Walker circulation over the WPWP, induces precipitation above 10 mm/day on average in the area (https://pmm.nasa.gov/TRMM/TRMM-based-climatology). At 140ºW, the interannual SSS signal amplitude reaches 1, which is twice the seasonal signal. Interannual SSS changes are due to variations of the surface freshwater fluxes but also of the ocean dynamics. Both horizontal and vertical processes have been shown to play an important role (Vialard et al. 2002 and Hasson et al., 2013ab, 2014, Gasparin et al. 2016, Qu et al., 2014). SSS was shown to be a robust tracer for ENSO (Delcroix and Picaut, 1998, Singh et al., 2011, Qu and Yu, 2014). Unlike SST, the ENSO signature in SSS is not only located within a few

93 degrees of the equator but reaches higher latitudes (Delcroix et al. 1998, Hasson et al. 2014).
94 This allows us to track the ENSO-related signal away from the Equator, something not
95 possible with SST because of the strong thermal air-sea coupling.
96 Studies have also underlined the active role of salinity in the tropical ocean dynamics through
97 its effect on the vertical density stratification. The presence of a haline stratification in the
98 WPFP, shallower than the thermal one, controls the mixed layer (ML) depth and creates
99 barrier layers (Lukas and Lindstrom, 1991, Sprintall and Tomczak, 1992, Qu et al., 2014).
100 The ocean responds to this salinity-controlled density stratification by decreasing entrainment
101 cooling and by intensifying the local response to wind stress. The westward South Equatorial
102 Current (SEC) brings saline water under the WPFP from the equatorial upwelling and
103 reinforces the barrier layer (Cronin and McPhaden, 2002). As the SEC is modulated by
104 ENSO, it induces a strong interannual variability of the barrier layer strength (Vialard and
105 Delecluse, 1998). SSS is found to play an active role in ENSO evolution (Ballabrera-Poy et
106 al., 2002, Vialard et al. 2002, Zhu et al. 2014) and a recent study found that the assimilation of
107 SSS in coupled forecasts yields longer ENSO predictability (Hackert et al., 2014).
108
109 Salinity is thus a unique tracer for tracking water mass displacement and as a rain gauge for
110 high rainfall areas (such as the ITCZ) but is also able to modulate sea-air interactions through
111 the formation of barrier layers.
112 Salinity has been extensively observed since the 2000s by the Argo program, with vertical
113 profiles from 5 to 2000 m depth (Roemmich et al., 2009). Since 2010, SSS is monitored at an
114 unprecedented resolution from space by the European satellite mission Soil Moisture Ocean
115 Salinity (SMOS), by the Argentinian-American satellite mission Aquarius and by the
116 American satellite mission Soil Moisture Active Passive (SMAP). These missions enable the
117 observation of SSS globally at a resolution between $50x50km^2$ and $150x150km^2$ every 3 to 8
118 days. More details on these are given in the Data/Methods Section of the present paper. This
119 suite of observations provides a unique opportunity for studying the interannual variability of
120 the upper ocean salinity with unprecedented details.
121
122 During the SMOS time period (2010-present), the Niño3.4 index reveals 2 distinct ENSO
123 phases (colored line, Fig. 2): one La Niña event (mid 2010-2011), a terminating El Niño event
124 (early 2010), a full El Niño event (mid 2015-mid 2016) and almost 3 years in a “neutral state”
125 (2012-2014). Indeed, SMOS started measuring surface salinity in 2010, just as a moderate El

Niño was finishing. Following this event, La Niña developed and lasted for about two years. SMOS observations of the 2010-2011 La Niña event show a strengthened WPFP eastern front and high salinity waters (above 35) reaching 150ºE at the equator (Fig. 2a). The strongest part of the signal is however found south of the equator in the SPCZ as was shown in a previous study by Hasson et al. 2013b.

The presence of El Niño precursors in early-2014 (McPhaden et al., 2015), suggested the development of a strong El Niño at the end of the year. However, the absence of sustained westerly wind events and unusually strong easterly winds in summer 2014 are thought to have halted the ongoing El Niño (McPhaden et al., 2015, Levine and McPhaden, 2016, Puy et al. 2016b, Zhu et al., 2016). Instead of shifting eastward, the WPWP remained west of the dateline and the lack of atmosphere-ocean coupling stalled the developing El Niño. During the following year, a major El Niño developed, to become one of the 3 strongest events ever measured since 1950 (Blunden and Arndt, 2016, Paek et al. 2017). The state of the tropical Pacific ocean at the end of 2014 has been suggested to have favored the outcome of this unusually strong El Niño event (Levine and McPhaden, 2016) even though the random occurrence of westward wind bursts can also explain its uniqueness (Puy et al. 2016b). By spring 2015, the SST increased in the central and eastern equatorial Pacific with a strong response of winds and atmospheric convection, leading to global atmospheric modifications (Palmeiro et al. 2017). Negative SSSA were observed between 0 and 15ºN around 170ºW from mid 2014 to mid 2015 (Boutin et al. 2016). This period was then followed by an acceleration of the El Niño development till early 2016. The atmospheric convection associated with the WPWP (i.e. the ascending branch of the Walker circulation) expanded east of the dateline and well above average precipitation were found in the central equatorial Pacific and south of the ITCZ, and below average near Indonesia.

By October 2015, and as expected, low salinities (below 35) and high temperatures were found around the equator east of the dateline (Fig. 2ab and 4) highlighting the El Niño eastward shift of the WPWP and WPFP described by Gasparin et al. (2016) and Corbett et al., (2017).

Additionally, significant freshening was observed around 20ºN (Fig. 2b and 4) accompanied with a slight increase in SST (Fig. 2d). While the equatorial SSS anomalies associated with past El Niño have been well documented, thanks, in particular, to the SSS observations of the TOGA/TAO network, the extra-equatorial anomalies less well known. This double anomalous

negative SSS feature appears to be specific to 2015. The extra-equatorial SSS anomaly is indeed not represented by the canonical SSS patterns associated with either the Central or Eastern Pacific El Niño events, as described by Singh et al. (2011) with 30 years of in situ observations (their Figure 5). The negative SSS anomaly associated with El Niño events of the observed period is located between 10ºN and 20ºS.

The 2015-2016 El Niño is the first event fully captured by the SMOS satellite mission, giving us an unprecedented opportunity to investigate the associated extra-equatorial SSSA. It is also the most powerful El Niño monitored by the fully deployed Argo program (Gasparin et al., 2016, Corbett et al., 2017). Guimbard et al. (2017) observed the extent of the EPFP (less than 34.5 in their study) to be 20% larger in 2015 than the climatology and to reach the dateline by the end of 2015. During the previous rainy season the preconditioning in 2014 of the zonal extension of the EPFP was found to be an essential factor enabling the development of the 2015 maxima.

In this paper we combine the analysis of satellite observations with a numerical simulation in order to investigate the unexpected 2015 northern tropical Pacific ocean SSS signal and the processes driving it. Data and methodology are presented in section 2. Section 3 presents the observation and analysis of the 2015 SSSA followed by the presentation of the mechanisms revealed from observation and modeling. Analogous events during the 1996-2014 period are also discussed. A discussion, conclusions and perspectives are given in section 4.

2. Data / Methods

This study is based on the combined use of observations (satellite, in situ) and a numerical simulation. All datasets and relevant characteristics are presented in this section.

2.1. Observational Datasets

SMOS satellite salinity and an optimal interpolation of Argo float salinity measurement datasets are at the center of our investigation.

The SMOS satellite mission was launched in November 2009 as the second European Space Agency (ESA) Earth Explorer (Kerr et al. 2010). It has been delivering space borne SSS since January 2010. The level-3 SMOS product used here is developed by the CATDS CEC-LOCEAN and known as debias_v2. This product is corrected for coastal biases following an improved method described in Kolodziejczyk et al. (2016) and for latitudinal biases (Boutin et al. 2017 in revision). This dataset is available on a 0.25x0.25º EASE grid, smoothed over 18 days and available every 4 days from January 2010 to the end of 2016. The accuracy of this SMOS SSS dataset in the open ocean is estimated to be better than 0.2 and is specifically assessed in our region in the present paper.

Numerous in situ SSS datasets are available. We use mooring datasets for their high temporal resolution timeseries available from the mid 90s at specific locations and an optimal interpolation of in situ observations (mainly Argo floats) for its synoptic coverage.

The TAO-TRITON array has been deployed in the tropical Pacific Ocean in order to study ENSO and its predictability following the 1982-1983 event. Moorings provides many high temporal resolution ocean and atmosphere measurements. Here, we use daily salinity and temperature measurements at various depth (McPhaden, 2006). As many moorings have gaps in their timeseries surface salinity and temperature data were also retrieved from the Woods Hole Oceanographic Institution Hawaii Ocean Timeseries Site (WHOTS) mooring at 22º 45'N, 158ºW. Mooring data is used in the present study for point-comparison of SSS and SST in order to assess other data quality. Whenever available, measurements from sensors at 1m depth were used and, when unavailable, the 10m depth sensor was used to get the longest possible time series. Stratification in the first 10 m is assumed to be negligible at the interannual time scale. Difference between the surface and 10m salinity can however sometimes reach 1 locally but on average the vertical salinity differences are -.03 in the tropics (Drucker and Riser, 2014) No flag was used for the TAO data as they were found to

be not fully reliable as shown by Tang et al. (2017). This is further explained in section 2.4. Only "Acceptable measurements" were used for WHOTS mooring.

The optimal interpolation "In Situ Analysis System" (ISAS) combines temperature and salinity measurements mainly from Argo floats profiles, TAO-TRITON moorings and vessels CTD casts. ISAS provides monthly fields of temperature and salinity from the surface ocean down to 2000m and on a near global .5°x.5° horizontal mesh (Gaillard et al., 2016). In this paper, we use the 5m depth level and version 6.2 of the ISAS algorithm applied in a delayed mode (with careful in situ data evaluation) until 2012 (Gaillard et al., 2016) and in near real-time data after 2012 (Brion et al., 2011). ISAS uses covariance scales of 300 km in longitude, proportional to the Rossby radius of deformation in latitude, and 30-day in time. The resolution of scales less than 300 km by the monthly gridded values is expected to be poor, even though it is weighted by the number of nearby data and their location.

Additional observational data have been used in order to study the mechanisms behind the observed salinity variations, amongst which the Sea Surface Temperature (SST) from the National Climatic Data Center of the National Oceanic and Atmospheric Administration (NODC/NOAA), the surface currents (U) from the Geostrophic and Ekman Current Observatory (GEKCO), evaporation (E) from Ocean-Atmosphere (OA)Flux and precipitation (P) from the Global Precipitation Climatology Project (GPCP).

The SST product is hereafter referred to as Reynolds SST (Reynolds et al., 2007). This gridded ¼-degree daily product (V2.0) is an optimal interpolation from combined datasets derived from satellites and in-situ data (from ships and buoys). Reynolds SST is available from 1981 till present. Based on satellite wind stress and altimeter sea level, GEKCO provides daily geostrophic and Ekman currents at a .25º spatial resolution from 1992 to present (Sudre et al. 2013). Currents within 2 degrees of the equator are discarded. GPCP precipitation data are available in its version 2.1 from October 1996 to October 2015 in a daily 2.5-degree resolution mesh (Huffman et al. 2009). The OAFlux project supplies evaporation data on a monthly 1° spatial grid from 1958 to present (Yu et al. 2008). Niño 3.4 SST anomalies were retrieved from the NOAA Earth Sciences Research Laboratory (ESRL) and subsequently smoothed by a 5-month moving average.

Nearly all in situ salinities are based on seawater conductivity providing Practical Salinity measurements. Even though the difference is not noticeable at our scale of interest in the tropical Pacific Ocean, all salinities have been converted into absolute salinities using the Thermodynamic Equation of Seawater (TEOS-10) established by the Intergovernmental

247 Oceanographic Comity (IOC) and are expressed in $g.kg^{-1}$ (IOC, SCOR and IAPSO, 2010).
248 Using absolute salinity allows a direct comparison of observations and model salinities
249 (Wright et al. 2011).

250

251 ## 2.2. Numerical simulation

252 To further analyze the SSSA associated with ENSO in 2015, forced oceanic experiments were
253 performed. The NEMO v3.2 model (Nucleus for European Modelling of the Ocean, Madec et
254 al., 2008) was set up in a 1° resolution global configuration (ORCA1, Hewitt et al., 2011),
255 with local transformations in the tropics leading to a 1/3° meridional resolution at the equator.
256 The model vertical resolution is 10m at the surface, 25m at 100m depth and 300m at 5000m
257 depth, resulting in 42 vertical levels. More details on the model configuration and assessment
258 can be found in Puy et al. (2016a). The numerical simulation provides daily outputs of all the
259 needed parameters for this study such as salinity, temperature and currents but also all the
260 terms of the mixed layer salinity budget equation (see Section 2.5).

261 The model is forced by the DRAKKAR Forcing Set v5.2 (DFS5.2, Dussin and Barnier 2013),
262 derived from ERA 40 (Uppala et al. 2005) until 2002 and ERA-Interim reanalysis (Dee et al.
263 2011) afterwards. The model is used in the present study to compute the salinity budget of the
264 mixed layer (ML) and therefore no direct SSS restoring can be used. In order to prevent the
265 salinity drift associated with the absence of restoring, a correcting term is computed as an
266 additional freshwater surface fluxes. This methodology was already used and described by
267 Vialard et al. (2002) and more recently by Hasson et al. (2013a, 2013b and 2014). The
268 computation of the correcting terms requires the run of a first simulation with a very strong
269 surface damping (i.e. 1000 mm/day). The 1985-2015 average correction on the freshwater
270 fluxes is computed from this first simulation and then added to the DFS5.2 forcing in the
271 second simulation. This way the simulation does not drift over time but keeps its dynamical
272 integrity for the time scales of interest. The correction corresponds to about 3.26% of the
273 average forcing field on our region of interest (10ºS-30ºN, 140ºE-70ºW). The ML salinity
274 budget is computed online at every model computation time step, the ML depth being defined
275 as the depth at which the density differs by 0.01 from the surface.

276 This model reproduces relatively well the interannual variability of the tropical Pacific Ocean
277 in 2014 and 2015 (Puy et al. 2016ab). The model is further assessed, especially in terms of
278 salinity, in Section 2.4.

2.3. Filtering time series

All anomalies were computed as described below. The common period of all datasets i.e. 2010-2015 is used to build a monthly climatology. Given the short length of the period, filtering the time series without excluding data on either end is challenging. Our first solution is to construct a monthly climatology is built from 25-month Butterworth high-pass filtered data. The difference between the climatology over the 2010-2015 and the full record period of each dataset is small and does not impact the results of this paper. This high-passed monthly climatology is then subtracted from the original dataset to create a first estimation of the interannual anomalies and is referred to as the "limited" interannual filter. This filtering methodology preserves each end of all time-series but does not filter out the intraseasonal variability. This "limited" interannual filter is used when investigating events close to the end of the time-series. A second solution uses the same processing but adds an additional 13-month low-pass filter to remove the residual high frequency variability and preserve the interannual variability. This more "robust" protocol is used whenever possible (i.e. 6-month away from either end of the time-series). Figure 3 shows interannual anomalies from the "limited" and "robust" filters from the 2010-2015 monthly climatology at two mooring sites (stars on Fig. 1a). Both filters remove the seasonal cycle adequately. As expected the "limited" filter leaves out some intraseasonal variability. This signal appears to be associated with waves such as tropical instability waves and barotropic Rossby waves (Kessler et al. 2006; Farrar 2011).

2.4. SSS datasets assessment

Comparison of the in situ, space-borne and simulated salinity datasets were made both at selected mooring positions and at the basin scale.

The coherence among the different products is estimated at several mooring sites in terms of SSS and SST. All datasets were compared to their closest neighbor and filtered using the "limited" and "robust" filters described above. This comparison is illustrated for SSS at the dateline-Equator TAO and the WHOTS moorings (stars on Fig. 1a; Fig. 3). All datasets in Fig. 3a show coherent variability in SSSA at the equator. TAO mooring timeseries suspiciously departs from other datasets by 0.5 in April 2003 highlighting possible issues with

311 the TAO data. Interannual SSS variations are however well represented, for instance during
312 ENSO phases (i.e. 1997, 2002, 2007, 2010 and 2015). Further north at WHOTS, observations
313 consistently show weaker variability than at lower latitude (Fig. 3b). SSS variations do not
314 show any apparent correlation with ENSO (Niño 3.4 index). We point out the strong
315 agreement between the mooring and SMOS SSS at both interannual and intraseasonal
316 timescales. The model shows stronger interannual variations. Moreover, the bathymetry
317 around the Hawaiian Islands, and thus currents, is very complex. The model is expected to
318 inaccurately represent the variability close to the islands.

319 In order to further assess the datasets, statistics at 18 moorings (stars and dots on Fig. 1a)
320 were computed (Table 1). Statistical comparisons were made for the TAO moorings Quality
321 Control (QC)'ed data and for the whole time-series regardless of the QC, and it was found 1)
322 that there were not enough QCed data points to compute significant comparisons at most
323 moorings and 2) the results presented below do not differ substantially whether non QCed
324 data is used or not. The TAO moorings measurement and the ISAS product are not strictly
325 independent but it is expected that the objective analysis of ISAS will smooth out large TAO
326 errors so it could be used to remove the largest errors in the TAO data. TAO minus ISAS SSS
327 Root Mean Square Deviation (RMSD) is used to test the TAO dataset. Wherever the TAO-
328 ISAS RMSD is larger than 0.3°C for SST and larger than 0.2 for SSS the TAO mooring
329 dataset is discarded. Filters described above are not used for this comparison. The mooring
330 data was averaged in time to reflect the other datasets time-resolution, leading to significant
331 differences in the number of points of comparison between datasets. Table 1 provides a
332 summary of the RMSD at the two moorings presented above (Fig. 3) and at all sites together.
333 NEMO- and Reynolds- TAO SST RMSD are below .5 and .4ºC respectively showing a good
334 accuracy of both means of SST. NEMO and SMOS reproduce accurately TAO measurements
335 (RMSD both around 0.25) even though some dubious measurements are still present in the
336 TAO dataset.

337 In order to further validate the large scale features which are of particular interest for the
338 present study, the October 2015 SSA is shown for SMOS, ISAS and the model in Figure 4
339 using the "limited filter". Patterns of the zonally-oriented basin-wide negative SSSA are
340 consistent amongst the products. Firstly, the structure of the strongest anomaly, centered
341 around the Equator and the dateline, is well simulated by the model when compared to both
342 observation datasets, although its eastward extent is slightly reduced. Secondly, a fresh tongue

extends eastwards from the first anomaly, centered around 8°N and 5° wide in latitude, as seen in SMOS observations and as reproduced well by the model. It is however very smooth and non-continuous in the ISAS optimal interpolation as expected from the product's effective resolution. Thirdly, the vast region of negative anomaly north of 10/15ºN is consistently seen in the model and in the observations. Finally, the patches of positive SSSA bracketed by the negative ones west of the dateline are also very coherent from one product to another. These features will be further described in the Results Section. The good agreement between in situ and SMOS SSS datasets is well known. Since satellites only measure the first cm of the water column and Argo top measurement is on average 5 m, stratification in the tropical areas can be substantial (see Boutin et al., 2016 for a review). It was however shown that at the large scale the impact of stratification is reduced (Druker and Riser, 2014). Differences in measurement methods must hence be kept in mind.

This assessment gives us confidence in the consistency of all datasets to reproduce the SSS interannual variability in the tropical Pacific Ocean, as described by the TAO moorings. It further shows the particular capacity of SMOS observations and model simulations to reproduce observed detailed structures such as the sharp frontal features that optimal interpolations, such as ISAS, struggle to represent.

2.5. Salinity Budget Processes

The ML salinity budget equation can be written as below (e.g. Hasson et al., 2013).

$$\underbrace{\partial_t \mathbf{S}}_{I} = \underbrace{(E-P)\frac{\mathbf{S}}{H}}_{II} + \underbrace{-\vec{u}\cdot\vec{\nabla}\mathbf{S}}_{III} + \underbrace{\vec{\nabla}\left(K_h\cdot\vec{\nabla}\mathbf{S}\right)}_{IV} + \underbrace{(w+\partial_t H)\frac{1}{H}\delta\mathbf{S}}_{V} + \underbrace{\partial_Z(K_z\cdot\delta\mathbf{S})\frac{1}{H}}_{VI} \quad (1)$$

Term *I* (g.kg^{-1}.year^{-1}) denotes the rate of change of salinity within the ML. The salinity averaged within the ML is denoted by **S**. The terms on the right-hand side of the equation describes the budget. Term *II* represents the freshwater forcing from the atmosphere onto the ML of depth H. The land freshwater contribution to the budget can be neglected in the tropical Pacific Ocean at the scales of interest. The horizontal processes are described by terms *III* and *IV*, which represent the advection by the ML horizontal currents and the horizontal mixing, respectively. Terms *V* and *VI* describe the vertical processes at the bottom

of the ML. The vertical advection and entrainment are represented by term *V*. Term *VI* corresponds to the vertical mixing. K_h and K_Z are the horizontal and vertical diffusion coefficients, and $\delta\mathbf{S}$ the vertical salinity gradient across the ML base.

Even though the processes at fine scales are parameterized by the diffusion coefficients, it is not possible to close this budget from observations only, given its complexity. All terms of the full salinity budget (Eq. 1) can be computed from the NEMO numerical simulation at every iteration step (online) except for the entrainment (residual). They are then averaged and archived daily.

Aside from the fine scales, the processes at depth within the ocean (e.g. at the bottom of the ML) are too complex to account for with in situ observations as shown by various studies (Hasson et al. 2013, Sommer et al 2015, Gasparin et al. 2016, Guimbard et al. 2017). The observation-based budget is therefore simplified as:

$$\underbrace{\partial_t \mathrm{SSS}}_{I} = \underbrace{(\mathrm{E}-\mathrm{P})\frac{\mathrm{SSS}}{\mathrm{H}}}_{II} + \underbrace{-\vec{u}\cdot\vec{\nabla}\mathrm{SSS}}_{III} + \text{residuals} \qquad (2)$$

Where the SSS and the surface currents (u) are assumed to be representative of the ML. All of the vertical and fine scale terms are included in the residuals (*IV, V, VI* of Equation 1) and only the SSS tendency (I), freshwater fluxes (II) and horizontal advection (III) are represented. Following the SMOS product resolution, the observation based budget is computed from 18-day low pass filtered data from which the median is computed within 2.5° of latitude and 5° of longitude to force all datasets to have the most consistent resolution and to smooth out the noise.

3. Results

3.1. The October 2015 20°N SSS anomaly

3.1.1. Description

By the end of 2015, significant freshening is observed around 20°N (Fig. 2c, Fig. 4). SSS decreases across the basin at this latitude from mid-2014 to 2016 (Fig. 2c). The EPFP edge, denoted by the "eastern" 35 isohaline, reaches the dateline. This basin-wide freshening is represented in all SSS observations and the model (Fig. 3b and 4) and has an amplitude greater than 0.5 between 10 and 25°N. This feature is hereafter referred to as the 20°N anomaly. It is accompanied by a large equatorial freshening of about 1 in the western part of

405 the basin, centered around the dateline (Fig. 2a and 4). Fresh waters (below 35) are found east
406 of the dateline from mid 2015 to mid 2016 and the two freshpools join one another (Fig. 2a).
407 As described in the introduction, the equatorial SSS decrease is associated with the eastward
408 shift of the WPFP associated with El Niño and was described by Gasparin et al. (2016) and
409 Corbett et al. (2017). The large equatorial negative SSSA (below -0.5) lies between 160ºE-
410 160ºW and 8ºS-8ºN with an extension spreading all the way to 90ºW and 10ºN, forming a
411 "sigma-shaped" pattern.
412
413 The two large-scale SSSAs are separated by a band of weaker anomalously fresh waters
414 centered around 10ºN. A positive +0.3 anomaly extends east from north of Papua New
415 Guinea to 170ºE (Fig. 4). This is consistent with Singh et al. (2011) analysis of El Niño
416 composite patterns of SSS.
417 This anomalous negative interannual SSS double-pattern (i.e. equatorial and extra-equatorial)
418 is specific to the year 2015. Singh et al. (2011) found SSSA associated with El Niño events to
419 be concentrated south of 10ºN. During the 2002-2003 and 2009-2010 El Niño events, no
420 freshening is found around 20ºN, both in ISAS, SMOS (2010 only) and modelling datasets
421 (Fig. 3b). In addition, the model does shows any significant freshening around 20ºN for any
422 of the simulated El Niño events during 1985-2013 (Fig. 3b).
423 In the present study, we show how the October 2015 20ºN SSS anomaly was generated and
424 how the equatorial and extra-equatorial anomaly are related.
425

426 ### 3.1.2. Build-up of the 20ºN SSS anomaly

427 The 20ºN SSS anomaly first appears in 2014 as shown by observation and modelling (Fig. 3b
428 and Fig. 2c). SSS decreases consistently amongst products at WHOTS mooring from early
429 2014 to the end of 2015 (Fig. 3b). The analysis of SMOS interannual monthly SSSA shows
430 that the 20ºN SSS anomaly appears to originate west of the dateline in the equatorial region in
431 early 2014 (Fig. 5a-d). The model simulation shows gradual build-up over 2014-2015 (Fig.
432 5e-h). The evolution of the April 2014 negative anomaly can be described from observations
433 and modelling as follows.
434 In April 2014, an equatorial negative interannual SSS anomaly of below -.3 is present west of
435 the dateline (Fig 5ae). From April to October 2014, SSS decreases across a large band,
436 roughly from 5 to 10ºN and from the dateline to the American coast. A zonal bipolar anomaly
437 is in place around the equator in October 2014 with an anomaly of -0.3 west of 170ºE and

+0.3 to the east (Fig. 5 bf). This "sigma shaped" anomaly resembles the canonical SSS signal associated with ENSO described by Singh et al. (2011), even if El Niño is not developing in 2014. By April 2015, the equatorial anomaly starts its eastward shift expected from the 2015 El Niño event development (Fig 5cg). North of 5ºN, the anomaly is intensified and spreads all the way to 20ºN. From April to October 2015, the negative equatorial anomaly intensifies to be well over -0.5 and reaches the dateline (Fig. 5dh). Similar to October 2014, the anomaly becomes "sigma shaped" as a narrow 5º-10ºN less fresh anomaly band develops. By October 2014, the positive anomaly centered on 5°S and the dateline has nearly disappeared to the east. The 20ºN anomaly (<-0.5) is distinct and spans from 10 to 25ºN (Fig. 5dh). The model shows a weaker anomaly than the observations but has consistent salinity patterns and timing. This discrepancy could be explained by very near surface stratification as the model averages salinity over the mixed layer (with a minimal depth of 10m, corresponding to the 1st level of the model) whereas SMOS measures the first centimeter. Moreover, this discrepancy can also be due to imprecision in the model's mixing parametrization and its coarser resolution north of 10ºN. Note that the equatorial Pacific Ocean is in a very similar state in April 2014 and April 2015 in terms of SSS (Fig. 5aecg). By October the difference between 2014 and 2015 is substantial. In 2015, the "sigma-shaped" anomaly fully develops and is seconded by the wide-spread 20ºN anomaly (Fig. 5dh). In early 2016, both anomalies weaken, even though the northward extension is still apparent (not shown).

During this period, saltier than usual waters occur off Baja California. This anomaly lasted all through 2014 and 2015 (Fig. 5a-d), which seems consistent with the warmer than usual waters found in this region at that time and called "the Blob" (Di Lorenzo and Mantua, 2016, Gentemann et al. 2017, Hu et al. 2017). Further exploration of this SSS anomaly and its relation to the "Blob" temperature anomaly are needed, but are beyond the scope of this study.

These strong interannual SSS variations are driven by freshwater fluxes (evaporation and precipitation) and the ocean currents and mixing through the salinity balance equation (Eq. 1). Freshwater fluxes are important in the region of interest with the strongest values (below -1.5 $m.yr^{-1}$) occurring in the ITCZ, South Pacific Convergence Zone (SPCZ) and WPWP regions, roughly between 5 and 10ºN across the basin and between 10ºS and 10ºN west of 170ºE (Fig. 1a). Freshwater fluxes have a strong variability at all timescales, which is evident from April 2014 to October 2015 (Fig. 5) and are consistent with SSSA to the first order, especially in

October 2014 and 2015. Discrepancies however underline the non-negligible role of ocean dynamics. North of 10ºN, the westward flowing North Equatorial Current (NEC) is the southern branch of the sub-tropical gyre (Fig. 1b, grey contours). The North Equatorial Counter-current (NECC) runs eastward between 3 and 10ºN with an average speed of .25 m/s. The SEC spans from 10ºS to 3ºN and is concentrated in two westward jets on each side of the equator of about .3 m/s speed. Trade winds not only force the zonal currents but also induces the equatorial upwelling and associated poleward meridional divergence called the Ekman drift. Tropical oceans have a short response time to atmospheric variations and therefore the currents system shows intense variability at seasonal and interannual time scales (Philander, 1990) as shown from April 2014 to October 2015 (Fig. 5, arrows). Patterns of SSSA and currents show an interesting coherence. It is however not straight forward how freshwater fluxes and surface currents interact to produce the observed SSS anomalies. Further investigation is performed in the following section, by considering the salinity budget over 2014-2015 from observations and modelling to shed light on the mechanisms leading to the 20ºN SSSA.

3.1.1. Associated Processes

Observations of SSS, freshwater fluxes and surface currents can provide an estimation of the SSS budget (Eq. 2) that can only represent surface processes (Fig. 6). The model on the other hand provides a full budget (Eq. 1) and provides details on the mechanisms that are unresolved by observations such as vertical processes (Fig. 7dhl).

Between April and October 2014, negative SSS tendencies are found between approximately 5º and 10ºN across the basin (Fig. 6a and 7a) leading to the narrow SSSA extension described above (Fig. 5bf). The observation budget shows that the freshwater fluxes do not account for all of this SSS decrease (Fig. 6, left column). East of 150ºW, the freshwater fluxes act to decrease the SSS north of the negative SSS tendency. The model confirms the role of advection which can only be indirectly inferred from observations (Fig. 7, left column). The SEC-induced advection increases SSS within 5º of the equator, whereas an intensified NECC brings fresher waters from the western part of the basin between 5º and 10ºN. The equatorial anomalous fresh waters associated with the 2014 weak El Niño are therefore advected by the NECC far into the center of the basin. Vertical processes have a damping effect on the SSS changes because of their dependence on the vertical stratification as described by Vialard et al. (2002) and Hasson et al. (2013a).

505 During the following 6-month period (October 2014 to April 2015) shows negative SSS
506 tendency north of 10ºN, corresponding to the 20ºN anomaly build-up. It is also accompanied
507 by the equatorial SSS decrease due to the developing 2015 El Niño event (Fig. 6 and 7,
508 central column). Observed and modelled freshwater fluxes are important during this period
509 but do not coincide with the northern SSS tendency as they are mostly damped by vertical
510 processes. In the model, horizontal advection appears to be the main driver of the SSS
511 decrease north of 10ºN brought by zonal currents (Fig. 7). Currents indeed drive low SSS
512 advected in the 5-10ºN area during the previous 6-month period to the north. Hasson et al.
513 (2014) found the Ekman drift to drive SSSA southward during the 2010-2011 La Niña in the
514 western tropical Pacific. It is hypothesized that the Ekman drift is also responsible for the
515 northward SSSA advection observed in 2014-2015. This hypothesis is further explored below.
516 This low SSS signal is not as affected as much by vertical processes as waters brought by the
517 zonal currents. As shown by Gasparin et al. (2016), horizontal advection and vertical
518 processes control the equatorial SSS decrease.
519 The 20ºN anomaly continues its build-up through the next 6-month period (Fig. 6 and 7, right
520 column). Negative SSS tendency is found within 10º of latitude of Hawaii. Similarly to the
521 previous period, the freshwater flux does not drive this SSS change as seen both for
522 observations and the model. If the analysis of observed horizontal advection does not allow to
523 draw any conclusions, the modelled advection clearly has an impact on the SSS tendency (Fig
524 7k). In mid 2015, El Niño is developing in the Pacific and the seasonal eastward flowing
525 NECC is in place whereas the SEC has nearly disappeared. The NECC reverts north into the
526 NEC around 100ºW, then flowing westward between 10º and 20ºN. As for the previous 6-
527 month period, we make the hypothesis that the Ekman drift is driving this northward
528 advection. Vertical processes are opposing horizontal advection north of Hawaii and help to
529 eventually dissipate the negative SSSA. During this period, the 20ºN anomaly appears in
530 conjunction with the canonical 10ºS-10ºN El Niño SSSA, with a strong negative tendency
531 between April and October 2015 and extending to the American continent. From April 2015,
532 El Niño develops and the entire atmospheric circulation is gradually modified, impacting
533 freshwater fluxes. Precipitation then increases across the tropical Pacific Ocean and especially
534 east of the WPWP climatological position and south of the ITCZ and SPCZ climatological
535 positions, leading to intense interannual surface freshwater fluxes across the tropical Pacific
536 ocean. Our budget confirms that a combination of all terms explains the associated equatorial
537 SSS decrease (Gasparin et al. 2016). North of Papua New-Guinea and in the Solomon Sea, the
538 effect of interannual freshwater forcing is positive, which is consistent with the modification

539 of the Walker circulation. A region of weakly increasing SSS is also present around 10°N
540 separating the two negative tendency regions. Modelled advection reveals the role of the
541 NECC advecting positive SSSA from the north of the Papua New-Guinea to the center of the
542 basin.
543
544 Analyzing the SSS budget over successive 6-month periods has enabled us to track the
545 sequence of processes leading to the unexpected 20ºN SSS anomaly observed and modelled in
546 October 2015. To summarize these processes, negative SSSAs are formed at the Equator,
547 west of the dateline, under El Niño conditions during January-April of the 2014 and 2015.
548 They are subsequently advected eastward between 5° and 10ºN by the NECC and amplified
549 by freshwater fluxes until October of each year. The 2014 and 2015 negative SSSAs continue
550 to be advected north but also zonally as the NECC retroflects to the north into the westward
551 flowing NEC. The SSSAs diminish as the seasonal NEC declines and are advected northward
552 reaching the Hawaiian Islands by April. They subsequently linger in the area. This cycle
553 happened twice, with the weak El Niño in 2014 and the strong event in 2015, and created the
554 unprecedented anomaly of October 2015.
555 It is however still not clear which mechanisms are behind the northward advection of the
556 equatorial SSSAs, whether it is specific to El Niño conditions and why it has not been
557 observed in the past. In order to investigate this, the longer records of SSS from SMOS, ISAS
558 and the model are now considered.
559

560 ## 3.2. Northward pathway of equatorial SSSA

561

562 At every occurrence of El Niño during the observed period (i.e. 2002-2003, 2009-2010 and
563 2014-2015) a negative SSS anomaly shows an apparent northward displacement between
564 150-170ºW (Fig. 8a-c). In addition, northward displacements of SSSAs also occur during
565 neutral periods, i.e. 2005 or 2007. Negative SSSAs are present at the equator west of 170ºW
566 during strong El Niño events especially in 1998 and 2015 when the equatorial anomaly
567 spreads eastward. During the 1997-1998 El Niño event and in the model, only a weak
568 anomaly reaches 20ºN early 2000. SSSAs in 2002, 2010 and 2014 only reach 170ºW at 5ºN
569 (Fig. 8a-c). In 2014, the SSSA is advected by the NECC eastward to 170ºW between 5° and
570 10ºN (Fig. 5c). The evolution of SSSA patterns from October 2002 to April 2004 and from
571 October 2009 to April 2011 (Fig. 9) is coherent with what has been described above for 2015

(Fig. 5). An equatorial anomaly is present west of the dateline in October of the first year. Six months later, the anomaly spans across the basin between 5 and 15ºN. The SSSAs become apparent between 150º-170ºW (Fig. 8a-c). In October of the second year, the anomaly begins its northward course and reaches 20ºN by April of the second year (Fig. 8a-c and Fig. 9).

To focus on this northward displacement the interannual SSS budget is computed from the model and presented as latitude-time plots averaged within 150-170ºW (Fig. 10). The SSS tendency shows the displacement of anomalies from 5-10ºN to 20-25ºN in about 18 months over the entire period (Fig. 10a) mirroring Figure 8c. Significant freshwater fluxes only occur south of 10ºN and do not show any northward displacement (Fig. 10b). The horizontal oceanic processes clearly appear as the main driver of the SSSA displacement (Fig. 10c). Vertical oceanic processes have a buffer effect on abrupt changes in SSS, resulting from surface fluxes and horizontal dynamics (Fig. 10f), as found in the 2014-2015 budget analysis.

In order to investigate in more detail the role of the different terms acting in the horizontal processes and to better understand the northward movement of SSSAs, the Ekman advection is computed off-line from the model as follows:

$$\underbrace{\vec{u} \cdot \vec{\nabla}\mathbf{S}}_{III} + \underbrace{\vec{\nabla}\left(\mathrm{K_h} \cdot \vec{\nabla}\mathbf{S}\right)}_{IV} = (\overrightarrow{u_e} + \overrightarrow{u_{ne}}) \cdot \vec{\nabla}\mathbf{S} + \underbrace{\vec{\nabla}\left(\mathrm{K_h} \cdot \vec{\nabla}\mathbf{S}\right)}_{IV}$$

$$= \underbrace{\overrightarrow{u_e} \cdot \vec{\nabla}\mathbf{S}}_{VII} + \underbrace{\overrightarrow{u_{ne}} \cdot \vec{\nabla}\mathbf{S}}_{VIII} + \underbrace{\vec{\nabla}\left(\mathrm{K_h} \cdot \vec{\nabla}\mathbf{S}\right)}_{IV} \quad (3)$$

Budget term numbers follow Equation 1, where III is the horizontal advection, IV is the horizontal mixing. VII represents the Ekman advection and VIII the non-Ekman advection (Fig. 10de). The Ekman current (u_e) is computed from the model wind and the non-Ekman current (u_{ne}) is the difference of u_e from the total current. Ekman currents are not computed within two degrees of the equator.

We hypothesized from the 2014-2015 budget analysis, that northward advection of SSSA is mostly driven by the Ekman currents. SSSAs are advected poleward throughout the 1996-2016 period, regardless of the ENSO phase of the ocean (Fig. 10cd). ENSO however modulates the 0-10ºN SSSA intensity (Singh et al., 2011) that is subsequently advected north (Fig. 8a-c). The large SSSA created by ENSO acts as a tracer to highlight the northward pathway described in the present study. This northward movement is further modulated by freshwater fluxes (Fig. 10b) as seen for instance in 2014-2015 when they reinforce the negative SSSA. Conversely, the 1997-1999 SSS budget suggests that the equatorial negative

anomaly advected north by the Ekman currents (Fig. 10d) is opposed by positive freshwater fluxes and vertical processes (Fig. 10bf). The 1997 El Niño event therefore triggered a strong freshening of the equatorial region that hardly appears at 20ºN.

Following their advection within the NECC (5-10ºN), the equatorial SSSAs continue their northward journey driven by the Ekman drift into the NEC (10-15ºN) and then northward out of NEC to around the latitude of the Hawaiian Islands (~20ºN) where they are slowly eroded.

4. Summary and conclusions

In 2015, an unusually large negative SSS basin-wide anomaly was measured at 20ºN in the Pacific ocean from space by the SMOS mission and in situ by Argo floats. In the same year, one of the strongest El Niño events on record developed and created disruptions in the atmospheric and oceanic circulations. The analysis of this 20ºN negative SSS anomaly reveals its origin almost 20 months earlier at the Equator. A sigma-shaped negative SSS anomaly centered on the Equator and the dateline is also observed in October 2015, as expected from the development of the 2015-2016 El Niño. This double-anomaly pattern at the equator and 20ºN was not found in the historical measurements of surface salinity during previous El Niño events. The mechanisms leading to this double anomaly were investigated here, using both in situ and satellite observations together with a validated ocean-only numerical simulation performed with the NEMO ocean model.

El Niño creates equatorial SSSA both via anomalous freshwater fluxes and modified ocean dynamics (advection, entrainment and mixing). The Walker circulation is strongly altered and its ascending branch is displaced and scattered from the western equatorial Pacific to a more central position. This leads to a modification of the precipitation patterns and of the trade winds over the Pacific Ocean, leading to changes in evaporation and in the equatorial currents system.

The SSS budget from observations provides the first key on the role of the surface processes described by Eq. 1. Observed surface freshwater forcing echoes the modifications in the Walker circulation in 2015. Even though the observed horizontal advection is noisy, some patterns can be distinguished but the results are too noisy to be quantified. Further analysis is conducted with the numerical simulation and confirms that horizontal advection is the main driver of SSS changes at the Equator. The WPFP is indeed advected eastward during the first 4 months of 2014 and 2015, driven by the weakening Trade winds and successive westerly wind events in 2015 (Puy et al., 2016b, Gasparin et al., 2016). During the following months,

these anomalies are further advected eastward by the NECC in a narrow band between 5 and 10ºN. Satellite observations and the model simulation (Fig. 5) indicate that the NECC intensity is particularly strong in 2015, as described by Guimbard et al., (2015; their Figure 12). The intensification of ITCZ precipitation between 5° and 10ºN associated with El Niño conditions from April to October 2015 also drives a strong decrease of SSS with a rate below -3 $year^{-1}$. A combination of surface advection and surface forcing is thus responsible for the narrow extension of the intense equatorial anomaly that extends zonally from the dateline to almost the American continent in October 2014 and 2015. The 5-10ºN SSSAs are subsequently advected north by the Ekman drift into the westward flowing NEC and then north out of it again. The westward advection of the EPFP does not appear to play a major role in the 5-10ºN SSS anomaly, as suggested by Guimbard et al. (2017).

The October 2014 SSSA is further advected North reaching 20ºN during the following year. Our analysis confirms that the Ekman drift acts as a basin-wide treadmill advecting these interannual anomalies poleward through the tropical zonal current system. Some part of the net northward transport of the SSSA is also carried by the NECC's retroflection northward into the NEC. Furthermore, smaller scale current features appear to interact with the Ekman northward drift, as revealed by the striking coherence of interannual SSSA and unfiltered surface currents for example around Hawaii (5-20ºN and 140-180ºW, Fig. 11) in both the model and observations. Cusps in the NECC and NEC are observed at these latitudes and it is hypothesized that they play a significant role in the northward displacement of the SSSA. They were described by Perigaut (1990) and Farrar and Weller (2006) as being baroclinic instability waves. Furthermore, they could transport anomalies in SST and SSS meridionally in a similar way to tropical instability waves near the equator (Kessler et al., 2006 and Lee et al., 2014). Note that the model SSSA structure is much smoother than the observations and may not resolve small scale eddies due to its 1° horizontal resolution at 20ºN. The cusps indeed create northward pathways for the fresh waters brought by the NECC from the western Pacific as seen in January 2015 (Fig. 11).

The present study demonstrates the importance of the Ekman drift, the NECC to NEC transport and suggests the role of smaller scale features in generating the October 2015 20ºN basin-wide SSSA as they all provide northward pathways for equatorial anomalies to reach the extra tropics. Analogous mechanisms occurred in the successive years in 2014 and 2015, led to a superimposition of SSSAs and created the unusually strong double structure in October 2015. Moreover, we find a strong anomaly by the end of 2016 (Fig. 2ac). The record of the past 20 years of observed and simulated SSS shows a continuous northward advection

of SSSA from the Equator to the Subtropics that is balanced by freshwater fluxes and vertical processes. This advection is particularly clear during El Niño events as anomalously strong SSSA are generated in the equatorial region. The 1997-1998 El Niño equatorial negative SSS anomaly was also advected north, but in this event it was counteracted by strong positive freshwater fluxes and vertical processes, especially in the ITCZ. The sequence of the halted 2014 El Niño producing a first equatorial SSS anomaly which was then reinforced by the ITCZ freshwater fluxes and lingered in the Pacific, then followed by El Niño conditions in 2015 led to the formation of the very large 20ºN anomaly in 2015.

In the recent years, the improvement of satellite SSS retrieval has enabled the study of the mean state and the variability of the SSS field at scales that are not resolved by the sparsely distributed very high frequency moorings, nor by the Argo network whose nominal resolution is about 300km and 10-day globally (Roemmich et al., 2009). The coherence of satellite-borne SSS and independent datasets such as altimetry currents gives us confidence in the quality of the data and their capacity to provide information at the large mesoscale. Both Argo profiling floats and TAO/TRITON moorings provide complementary *in situ* datasets giving valuable insight into subsurface processes that cannot be observed from space (Gasparin et al. 2015) and provide a benchmark of in situ observations for the calibration and validation of space missions as well as models. Their first order importance should not be disregarded and this complementary observing capacity needs to be maintained in the future (Durack et al. 2016).

This study shows the ability of SSS to retain El Niño-generated anomalies for up to 20 months from the equator to 20ºN, in striking contrast to SST (Figure 8cd) which is rapidly eroded by air-sea interactions. This close-to-passive behavior is another testimony of the central role of salinity as an essential tracer to understand the ocean and its role in climate.

Acknowledgements

AH acknowledges the support of a CNES Postdoctoral fellowship. This work is a contribution to the TOSCA/ SMOS-Ocean proposal supported by CNES. We benefited from numerous datasets made freely available and are listed here: The SMOS debias_v2 SSS produced by LOCEAN/IPSL (UMR CNRS/UPMC/IRD/ MNHN,) laboratory which participates in the Ocean Salinity Expertise Center (CECOS) of Centre Aval de Traitement des Donnees SMOS (CATDS) at IFREMER, Plouzane, France (http://www.catds.fr/Products, see documentation : http://www.catds.fr/Products/Available-products-from-CEC-OS/L3-Debiased-Locean-v2);

the TAO-TRITON moorings data by GTMBA Project Office of NOAA/PMEL (https://www.pmel.noaa.gov/gtmba/); the WHOTS mooring supported by NOAA through the Cooperative Institute for Climate and Ocean Research (CICOR) and by National Science; the in situ Analysis System (ISAS) by LPO (CNRS/ IFREMER/IRD/UBO) and products were made available by F. Gaillard (wwz.ifremer.fr/lpo/La-recherche/Projets- en-cours/GLOSCAL), the Precipitation Climatology Project data (http://www.esrl.noaa.gov/psd/data/gridded/data.gpcp.html), Nino 3.4 Index (https://www.esrl.noaa.gov/psd/gcos_wgsp/Timeseries/Nino34/), Woods Hole Oceanographic Institution OAFlux evaporation dataset (http://oaflux.whoi.edu/evap.html), GEKCO product by Joël Sudre at LEGOS, France (http://ctoh.legos.obs-mip.fr/products/global-surface-currents/global-surface-current-data-product) and Reynolds SST (ftp://eclipse.ncdc.noaa.gov/pub/OI-daily-v2/NetCDF//). We acknowledge the support of the Belmont project GOTHAM, under grant ANR-15-JCLI-0004-01. We thank Jérôme Vialard for some very helpful discussions.

References

Alory, G., Maes, C., Delcroix, T., Reul, N., & Illig, S. (2012). Seasonal dynamics of sea surface salinity off Panama: The far Eastern Pacific Fresh Pool. *Journal of Geophysical Research: Oceans*, *117*(C4), C04028. https://doi.org/10.1029/2011JC007802

Ballabrera-Poy, J., Murtugudde, R., & Busalacchi, A. J. (2002). On the potential impact of sea surface salinity observations on ENSO predictions. *Journal of Geophysical Research-Oceans*, *107*(C12). https://doi.org/10.1029/2001jc000834

Blunden, J., & Arndt, D. S. (2016). State of the Climate in 2015. *Bulletin of the American Meteorological Society*, *97*(8), Si-S275. https://doi.org/10.1175/2016BAMSStateoftheClimate.1

Bosc, C., Delcroix, T., & Maes, C. (2009). Barrier layer variability in the western Pacific warm pool from 2000 to 2007. *Journal of Geophysical Research-Oceans*, *114*. https://doi.org/10.1029/2008jc005187

Boutin, J., Martin, N., Kolodziejczyk, N., & Reverdin, G. (2016). Interannual anomalies of SMOS sea surface salinity. *Remote Sensing of Environment*, *180*, 128–136. https://doi.org/10.1016/j.rse.2016.02.053

Boutin, J., Chao, Y., Asher, W. E., Delcroix, T., Drucker, R., Drushka, K., … Ward, B. (2016). Satellite and In Situ Salinity: Understanding Near-Surface Stratification and Subfootprint Variability. *Bulletin of the American Meteorological Society*, *97*(8), 1391–1407. https://doi.org/10.1175/BAMS-D-15-00032.1

Brion, E., Gaillard, F., Petit de la Villéon, L., Delcroix, T., Alory, G., & Reverdin, G. (2011). Collecting and gridding complementary in-situ SST/SSS data for the calibration and validation of SMOS, *41*, 33.

Corbett, C. M., Subrahmanyam, B., & Giese, B. S. (2017). A comparison of sea surface salinity in the equatorial Pacific Ocean during the 1997–1998, 2012–2013, and 2014–2015 ENSO events. *Climate Dynamics*. https://doi.org/10.1007/s00382-017-3527-y

Cronin, M. F., & McPhaden, M. J. (2002). Barrier layer formation during westerly wind bursts. *Journal of Geophysical Research-Oceans*, *107*(C12). https://doi.org/10.1029/2001jc001171

752 Dee, D. P., Uppala, S. M., Simmons, A. J., Berrisford, P., Poli, P., Kobayashi, S., … Vitart, F.
753 (2011). The ERA-Interim reanalysis: configuration and performance of the data
754 assimilation system. *Quarterly Journal of the Royal Meteorological Society*,
755 *137*(656), 553–597. https://doi.org/10.1002/qj.828
756 Delcroix, T., Gourdeau, L., & Henin, C. (1998). Sea surface salinity changes along the Fiji-
757 Japan shipping track during the 1996 La Nina and 1997 El Nino period.
758 *Geophysical Research Letters*, *25*(16), 3169–3172.
759 https://doi.org/10.1029/98gl02320
760 Delcroix, T., & Picaut, J. (1998). Zonal displacement of the western equatorial Pacific "fresh
761 pool." *Journal of Geophysical Research-Oceans*, *103*(C1), 1087–1098.
762 https://doi.org/10.1029/97jc01912
763 Di Lorenzo, E., & Mantua, N. (2016). Multi-year persistence of the 2014/15 North Pacific
764 marine heatwave. *Nature Clim. Change*, *6*(11), 1042–1047.
765 https://doi.org/10.1038/nclimate3082
766 Drucker, R., & Riser, S. C. (2014). Validation of Aquarius sea surface salinity with Argo:
767 Analysis of error due to depth of measurement and vertical salinity stratification.
768 *Journal of Geophysical Research: Oceans*, *119*(7), 4626–4637.
769 https://doi.org/10.1002/2014JC010045
770 Durack, P. J., Lee, T., Vinogradova, N. T., & Stammer, D. (2016). Keeping the lights on for
771 global ocean salinity observation. *Nature Clim. Change*, *6*(3), 228–231.
772 https://doi.org/10.1038/nclimate2946
773 Dussin, R., & Barnier, B. (2013). The making of DFS 5.1. *Drakkar Project Rep*.
774 Farrar, J. T. (2011). Barotropic Rossby Waves Radiating from Tropical Instability Waves in
775 the Pacific Ocean. *Journal of Physical Oceanography*, *41*(6), 1160–1181.
776 https://doi.org/10.1175/2011JPO4547.1
777 Farrar, J. T., & Weller, R. A. (2006). Intraseasonal variability near 10 N in the eastern tropical
778 Pacific Ocean. *Journal of Geophysical Research: Oceans*, *111*(C5).
779 Gaillard, F., Reynaud, T., Thierry, V., Kolodziejczyk, N., & von Schuckmann, K. (2016). In
780 Situ–Based Reanalysis of the Global Ocean Temperature and Salinity with ISAS:
781 Variability of the Heat Content and Steric Height. *Journal of Climate*, *29*(4), 1305–
782 1323. https://doi.org/10.1175/JCLI-D-15-0028.1
783 Gasparin, F., & Roemmich, D. (2016). The strong freshwater anomaly during the onset of the
784 2015/2016 El Niño. *Geophysical Research Letters*, *43*(12), 6452–6460.
785 https://doi.org/10.1002/2016GL069542

786 Gentemann, C. L., Fewings, M. R., & García-Reyes, M. (2017). Satellite sea surface
787 temperatures along the West Coast of the United States during the 2014–2016
788 northeast Pacific marine heat wave. *Geophysical Research Letters*, *44*(1), 312–319.
789 https://doi.org/10.1002/2016GL071039
790 Gordon, A. L., Giulivi, C. F., Busecke, J., & Bingham, F. M. (2015). Differences among
791 subtropical surface salinity patterns. *Oceanography*, *28*(1), 32–39.
792 Gouriou, Y., & Delcroix, T. (2002). Seasonal and ENSO variations of sea surface salinity and
793 temperature in the South Pacific Convergence Zone during 1976-2000. *Journal of*
794 *Geophysical Research-Oceans*, *107*(C12). https://doi.org/10.1029/2001jc000830
795 Guimbard, S., Reul, N., Chapron, B., Umbert, M., & Maes, C. (2017). Seasonal and
796 interannual variability of the Eastern Tropical Pacific Fresh Pool. *Journal of*
797 *Geophysical Research: Oceans*, *122*(3), 1749–1771.
798 https://doi.org/10.1002/2016JC012130
799 Hackert, E., Busalacchi, A. J., & Ballabrera-Poy, J. (2014). Impact of Aquarius sea surface
800 salinity observations on coupled forecasts for the tropical Indo-Pacific Ocean.
801 *Journal of Geophysical Research: Oceans*, *119*(7), 4045–4067.
802 https://doi.org/10.1002/2013JC009697
803 Hasson, A., Delcroix, T., Boutin, J., Dussin, R., & Ballabrera-Poy, J. (2014). Analyzing the
804 2010–2011 La Niña signature in the tropical Pacific sea surface salinity using in
805 situ data, SMOS observations, and a numerical simulation. *Journal of Geophysical*
806 *Research: Oceans*, *119*(6), 3855–3867. https://doi.org/10.1002/2013JC009388
807 Hasson, A., Delcroix, T., & Boutin, J. (2013). Formation and variability of the South Pacific
808 Sea Surface Salinity maximum in recent decades. *Journal of Geophysical*
809 *Research-Oceans*, *118*(10), 5109–5116. https://doi.org/10.1002/jgrc.20367
810 Hasson, Delcroix, T., & Dussin, R. (2013). An assessment of the mixed layer salinity budget
811 in the tropical Pacific Ocean. Observations and modelling (1990-2009). *Ocean*
812 *Dynamics*, *63*(2–3), 179–194. https://doi.org/10.1007/s10236-013-0596-2
813 Hewitt, H. T., Copsey, D., Culverwell, I. D., Harris, C. M., Hill, R. S. R., Keen, A. B., …
814 Hunke, E. C. (2011). Design and implementation of the infrastructure of
815 HadGEM3: the next-generation Met Office climate modelling system. *Geosci.*
816 *Model Dev.*, *4*(2), 223–253. https://doi.org/10.5194/gmd-4-223-2011
817 Hu, Z.-Z., Kumar, A., Jha, B., Zhu, J., & Huang, B. (2017). Persistence and Predictions of the
818 Remarkable Warm Anomaly in the Northeastern Pacific Ocean during 2014–16.
819 *Journal of Climate*, *30*(2), 689–702. https://doi.org/10.1175/JCLI-D-16-0348.1

820 Huffman, G. J., Adler, R. F., Bolvin, D. T., & Gu, G. (2009). Improving the global
821 precipitation record: GPCP Version 2.1. *Geophysical Research Letters*, *36*(17), n/a-
822 n/a. https://doi.org/10.1029/2009GL040000
823 Kao, H.-Y., & Lagerloef, G. S. E. (2015). Salinity fronts in the tropical Pacific Ocean.
824 *Journal of Geophysical Research-Oceans*, *120*(2), 1096–1106.
825 https://doi.org/10.1002/2014jc010114
826 Kerr, Y. H., Waldteufel, P., Wigneron, J.-P., Delwart, S., Cabot, F., Boutin, J., …
827 Mecklenburg, S. (2010). The SMOS Mission: New Tool for Monitoring Key
828 Elements of the Global Water Cycle. *Proceedings of the Ieee*, *98*(5), 666–687.
829 https://doi.org/10.1109/jproc.2010.2043032
830 Kessler, W. S. (2006). The circulation of the eastern tropical Pacific: A review. *Progress in*
831 *Oceanography*, *69*(2–4), 181–217. https://doi.org/10.1016/j.pocean.2006.03.009
832 Kolodziejczyk, N., Boutin, J., Vergely, J.-L., Marchand, S., Martin, N., & Reverdin, G.
833 (2016). Mitigation of systematic errors in SMOS sea surface salinity. *Remote*
834 *Sensing of Environment*, *180*, 164–177. https://doi.org/10.1016/j.rse.2016.02.061
835 Lee, T., Lagerloef, G., Kao, H.-Y., McPhaden, M. J., Willis, J., & Gierach, M. M. (2014). The
836 influence of salinity on tropical Atlantic instability waves. *Journal of Geophysical*
837 *Research: Oceans*, *119*(12), 8375–8394. https://doi.org/10.1002/2014JC010100
838 Levine, A. F. Z., McPhaden, M. J., & Frierson, D. M. W. (2017). The impact of the AMO on
839 multidecadal ENSO variability: AMO IMPACTS ON ENSO. *Geophysical*
840 *Research Letters*, *44*(8), 3877–3886. https://doi.org/10.1002/2017GL072524
841 Lukas, R., & Lindstrom, E. (1991). The Mixed Layer of the Western Equatorial Pacific
842 Ocean. *Journal of Geophysical Research-Oceans*, *96*, 3343–3357.
843 Madec, G. (2008). NEMO ocean engine, *Note du Pole de Modélisation*(27), 300.
844 Maes, C., Reul, N., Behringer, D., & O'Kane, T. (2014). The salinity signature of the
845 equatorial Pacific cold tongue as revealed by the satellite SMOS mission.
846 *Geoscience Letters*, *1*(1). https://doi.org/10.1186/s40562-014-0017-5
847 McPhaden, M. J., Zebiak, S. E., & Glantz, M. H. (2006). ENSO as an integrating concept in
848 earth science. *Science*, *314*(5806), 1740–1745.
849 McPhaden, M. J., Timmermann, A., Widlansky, M. J., Balmaseda, M. A., & Stockdale, T. N.
850 (2015). The curious case of the El Niño that never happened: a perspective from 40
851 years of progress in climate research and forecasting. *Bulletin of the American*
852 *Meteorological Society*, *96*(10), 1647–1665.

Paek, H., Yu, J.-Y., & Qian, C. (2017). Why were the 2015/2016 and 1997/1998 extreme El Niños different? *Geophysical Research Letters*, *44*(4), 1848–1856. https://doi.org/10.1002/2016GL071515

Palmeiro, F. M., Iza, M., Barriopedro, D., Calvo, N., & García-Herrera, R. (2017). The complex behavior of El Niño winter 2015–2016. *Geophysical Research Letters*, *44*(6), 2902–2910. https://doi.org/10.1002/2017GL072920

Périgaud, C. (1990). Sea level oscillations observed with Geosat along the two shear fronts of the Pacific North Equatorial Countercurrent. *Journal of Geophysical Research: Oceans*, *95*(C5), 7239–7248. https://doi.org/10.1029/JC095iC05p07239

Philander, S. G., Holton, J. R., & Dmowska, R. (1989). *El Nino, La Nina, and the Southern Oscillation*. Elsevier Science. Retrieved from http://books.google.fr/books?id=9fwrkW_B1YYC

Puy, M., Vialard, J., Lengaigne, M., & Guilyardi, E. (2016). Modulation of equatorial Pacific westerly/easterly wind events by the Madden–Julian oscillation and convectively-coupled Rossby waves. *Climate Dynamics*, *46*(7), 2155–2178. https://doi.org/10.1007/s00382-015-2695-x

Puy, M., Vialard, J., Lengaigne, M., Guilyardi, E., Voldoire, A., & Madec, G. (2016). Modulation of equatorial Pacific sea surface temperature response to westerly wind events by the oceanic background state. *Climate Dynamics*. https://doi.org/10.1007/s00382-016-3480-1

Qu, T., Song, Y. T., & Maes, C. (2014). Sea surface salinity and barrier layer variability in the equatorial Pacific as seen from Aquarius and Argo: SEA SURFACE SALINITY AND BARRIER LAYER. *Journal of Geophysical Research: Oceans*, *119*(1), 15–29. https://doi.org/10.1002/2013JC009375

Qu, T., & Yu, J.-Y. (2014). ENSO indices from sea surface salinity observed by Aquarius and Argo. *Journal of Oceanography*, *70*(4), 367–375. https://doi.org/10.1007/s10872-014-0238-4

Reynolds, R. W., Smith, T. M., Liu, C., Chelton, D. B., Casey, K. S., & Schlax, M. G. (2007). Daily high-resolution-blended analyses for sea surface temperature. *Journal of Climate*, *20*(22), 5473–5496. https://doi.org/10.1175/2007jcli1824.1

Roemmich, D., Johnson, G. C., Riser, S., Davis, R., Gilson, J., Owens, W. B., … Ignaszewski, M. (2009). The Argo Program: Observing the global ocean with profiling floats. *Oceanography*, *22*(2), 34–43.

886 Sarachik, E. S., and Mark A. Cane. (2010). *The El Niño-Southern Oscillation Phenomenon*.
887 Cambridge University Press.
888 Singh, A., Delcroix, T., & Cravatte, S. (2011). Contrasting the flavors of El Nino-Southern
889 Oscillation using sea surface salinity observations. *Journal of Geophysical*
890 *Research-Oceans*, *116*. https://doi.org/10.1029/2010jc006862
891 Sommer, A., Reverdin, G., Kolodziejczyk, N., & Boutin, J. (2015). Sea Surface Salinity and
892 Temperature Budgets in the North Atlantic Subtropical Gyre during SPURS
893 Experiment: August 2012-August 2013. *Frontiers in Marine Science*, *2*, 107.
894 https://doi.org/10.3389/fmars.2015.00107
895 Sprintall, J., & Tomczak, M. (1992). Evidence of the barrier layer in the surface layer of the
896 tropics. *Journal of Geophysical Research*, *97*(C5), 7305.
897 https://doi.org/10.1029/92JC00407
898 Sudre, J., Maes, C., & Garçon, V. (2013). On the global estimates of geostrophic and Ekman
899 surface currents. *Limnology and Oceanography: Fluids and Environments*, *3*(1), 1–
900 20.
901 Takahashi, K., Martínez, R., Montecinos, A., Dewitte, B., Gutiérrez, D., & Rodríguez-Rubio,
902 E. (2014). White Paper# 8a—Regional applications of observations in the eastern
903 Pacific: Western South America. Report of the Tropical Pacific Observing System
904 2020 Workshop (TPOS 2020) GCOS-184.
905 Tang, W., Fore, A., Yueh, S., Lee, T., Hayashi, A., Sanchez-Franks, A., … Baranowski, D.
906 (2017). Validating SMAP SSS with in situ measurements. *Remote Sensing of*
907 *Environment*, *200*, 326–340. https://doi.org/10.1016/j.rse.2017.08.021
908 Tchilibou, M., Delcroix, T., Alory, G., Arnault, S., & Reverdin, G. (2015). Variations of the
909 tropical Atlantic and Pacific SSS minimum zones and their relations to the ITCZ
910 and SPCZ rain bands (1979-2009). *Journal of Geophysical Research-Oceans*,
911 *120*(7), 5090–5100. https://doi.org/10.1002/2015jc010836
912 Uppala, S. M., Kållberg, P., Simmons, A., Andrae, U., Bechtold, V. d, Fiorino, M., … Kelly,
913 G. (2005). The ERA-40 re-analysis. *Quarterly Journal of the Royal Meteorological*
914 *Society*, *131*(612), 2961–3012.
915 Vialard, J., & Delecluse, P. (1998). An OGCM study for the TOGA decade. Part II: Barrier-
916 layer formation and variability. *Journal of Physical Oceanography*, *28*(6), 1089–
917 1106. https://doi.org/10.1175/1520-0485(1998)028<1089:aosftt>2.0.co;2

Vialard, J., Delecluse, P., & Menkes, C. (2002). A modeling study of salinity variability and its effects in the tropical Pacific Ocean during the 1993–1999 period. *Journal of Geophysical Research: Oceans*, *107*(C12).

Wang, C., & Picaut, J. (2004). Understanding ENSO physics—A review. *Earth's Climate*, 21–48.

Wright, D., Pawlowicz, R., McDougall, T., Feistel, R., & Marion, G. (2011). Absolute Salinity,''Density Salinity''and the Reference-Composition Salinity Scale: present and future use in the seawater standard TEOS-10. *Ocean Science*, *7*(1), 1–26.

Yu. (2011). A global relationship between the ocean water cycle and near-surface salinity. *Journal of Geophysical Research*, *116*(C10). https://doi.org/10.1029/2010JC006937

Yu, L. (2015). Sea-surface salinity fronts and associated salinity-minimum zones in the tropical ocean. *Journal of Geophysical Research: Oceans*, *120*(6), 4205–4225.

Yu, L., Jin, X., & Weller, R. A. (2008). *Multidecade Global Flux Datasets from the Objectively Analyzed Air-sea Fluxes (OAFlux) Project: Latent and sensible heat fluxes, ocean evaporation, and related surface meteorological variables*. (OAFlux Project Technical Report) (p. 64pp.). Woods Hole Massachusetts: Woods Hole Oceanographic Institution.

Zhu, J., Huang, B., Zhang, R.-H., Hu, Z.-Z., Kumar, A., Balmaseda, M. A., … Kinter III, J. L. (2014). Salinity anomaly as a trigger for ENSO events. *Scientific Reports*, *4*.

Zhu, J., Kumar, A., Huang, B., Balmaseda, M. A., Hu, Z.-Z., Marx, L., & Kinter III, J. L. (2016). The role of off-equatorial surface temperature anomalies in the 2014 El Niño prediction. *Scientific Reports*, *6*(1). https://doi.org/10.1038/srep19677

Figure Captions

Table 1. Root mean square differences (RD) between Mooring observations (selected TAO, WHOTS and all TAO and WHOTS) and the model (NEMO), interpolated in situ (ISAS), interpolated in situ and satellite (Reynolds) and satellite only (SMOS) data, in terms of sea surface temperature and salinity.

Figure 1. 2010-2016 mean fields of (a) SSS (SMOS) and freshwater flux (0 and -1.5 m.yr-1 contours, OAFlux and GPCP) and (b) current velocity and associated streamlines

951 (GEKCO). Stars and dots denotes moorings used to produce Table 1. Timeseries
952 from moorings denoted by stars at shown on Fig. 3.
953 Figure 2. 2010-2016 longitude-time plots of SSS (SMOS) averaged between 2ºS and 2ºN (a)
954 and 16 and 20ºN (c) and of SST (Reynolds) averaged between 2ºS and 2ºN (b) and
955 18 and 22ºN (d). NINO3.4 on top of all panels, blue during La Niña and red during
956 El Nino.
957 Figure 3. Time series of monthly interannual SSS at (a) the equator and 180ºE and (b) at
958 158ºW, 23ºN from Moorings (green), ISAS (red), SMOS SSS (yellow) and the
959 NEMO numerical simulation (blue). Lighter colors and thinner lines for the
960 seasonal climatology anomaly (limited filter) and darker thicker lines when using
961 the "robust" filter. The dashed grey line denotes the Niño 3.4 index (-.4 scaling).
962 Figure 4. October 2015 SSS Interannual Anomaly from (a) SMOS, (b) ISAS and (c) the
963 model from the "limited" filtering technique.
964 Figure 5. Monthly average, every 6 months, of the interannual SMOS (a-d, left panels) and
965 modelled (e-h, right panels) SSS anomaly (color), unfiltered currents (arrows) and
966 isohyets (-2.5 and -3.5 m.yr-1, magenta contours) for the months of April and
967 October 2014 and 2015.
968 Figure 6. 7-month SSS tendency (a, d, g), fresh water fluxes (b, e, h) and horizontal (c, h, i)
969 advection centered around July 2014 (a-c, left panels), January 2015 (d-f, middle
970 panels) and July 2015 (g-I, right panels) from observations. Panels a, d and g
971 represent SSS changes (Term I of Eq. 2) from April 2014 (Fig. 5a) to October 2014
972 (Fig. 5b), from October 2014 (Fig. 5b) to April 2015 (Fig. 5c) and from April 2015
973 (Fig. 5c) to October 2015 (Fig. 5d) respectively. SSS changes associated with
974 freshwater fluxes and horizontal advection (Terms II and III of Eq. 2) over the same
975 periods are shown on panels b, e, h and c, h, i respectively. Contours on all panels
976 represent the -0.1 year-1 SSS tendency for each period.
977 Figure 7. 7-month SSS tendency (a, e, i), fresh water fluxes (b, f, j), horizontal (c, g, k) and
978 vertical (d, h, l) ocean processes centered around July 2014 (a-d, left panels),
979 January 2015 (e-h, middle panels) and July 2015 (i-l, right panels) from the NEMO
980 numerical simulation. Contours on all panels represent the -0.1 year-1 SSS
981 tendency for each period. Analogous to Figure 6.
982 Figure 8. 150º-170ºW Latitude-time plot of the interannual SSS anomaly from SMOS (a),
983 ISAS (b), and NEMO (c) and SST from NEMO (d). NINO3.4 on top of all panels,
984 blue during La Niña and red during El Nino (scaled by -2, centered on the Equator).

Figure 9. Interannual NEMO SSS anomaly for the months of October 2002 (a), April and October 2003 (b, c), April 2004 (d), October 2009 (e), April and October 2010 (f,g) and April 2011(h).

Figure 10. 150º-170ºW latitude-time plots of the interannual NEMO SSS budget as described by Equations 1 and 3: (a) SSS tendency, (b) freshwater fluxes, (c) horizontal processes, (d) Ekman horizontal advection, (e) remaining horizontal processes from the Ekman horizontal advection and (f) vertical processes

Figure 11. SSSA and currents from (a) SMOS and (b) NEMO for January 2015

Tables

Table 1. Root mean square differences (RD) between Mooring observations (selected TAO and WHOTS moorings (same as Fig. 3) and all TAO and WHOTS) and the model (NEMO), interpolated in situ (ISAS), interpolated in situ and satellite (Reynolds) and satellite only (SMOS) data, in terms of sea surface temperature and salinity.

	Sea Surface Temperature (ºC)						**Sea Surface Salinity**					
	NEMO		ISAS		Reynolds		NEMO		ISAS		SMOS	
	N	RD	N	RD	N	RD	N	RD	N	RD	N	RD
TAO	6805	0.60	161	0.27	1614	0.45	5904	0.33	135	0.19	354	0.33
WHOTS	3980	0.35	131	0.16	1073	0.24	3980	0.25	131	0.22	200	0.18
All	62756	0.48	1445	0.24	14638	0.37	41045	0.28	1203	0.15	3987	0.24

Figures

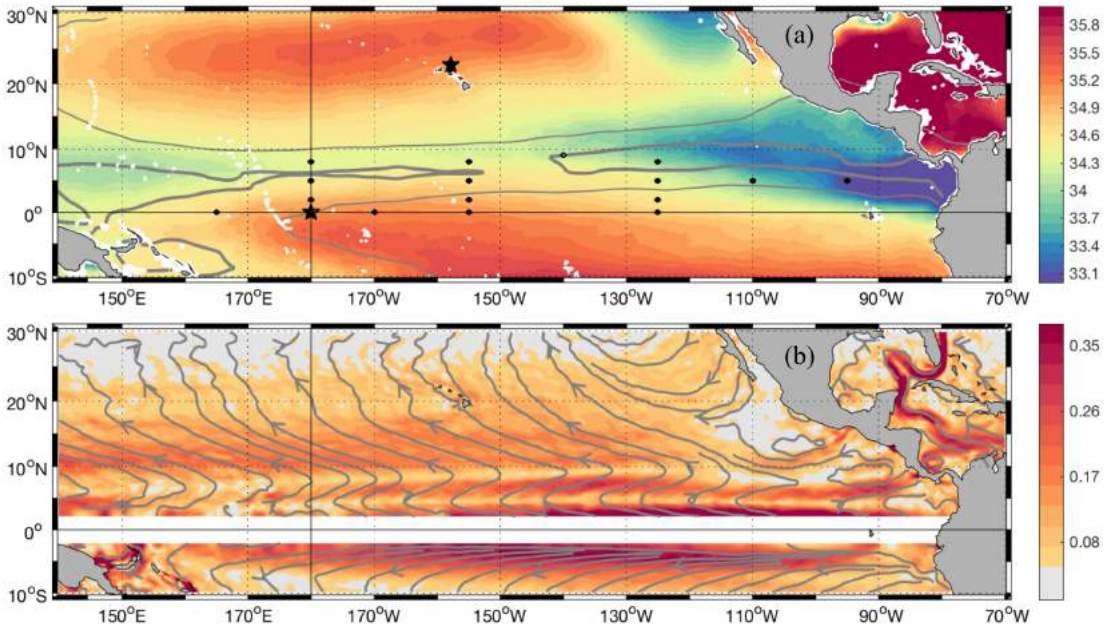

Figure 1. 2010-2016 mean fields of (a) SSS (SMOS) and freshwater flux (0 and -1.5 m.yr-1 contours, OAFlux and GPCP) and (b) current velocity and associated streamlines (GEKCO). Stars and dots denotes moorings used to produce Table 1. Timeseries from moorings denoted by stars at shown on Fig. 3.

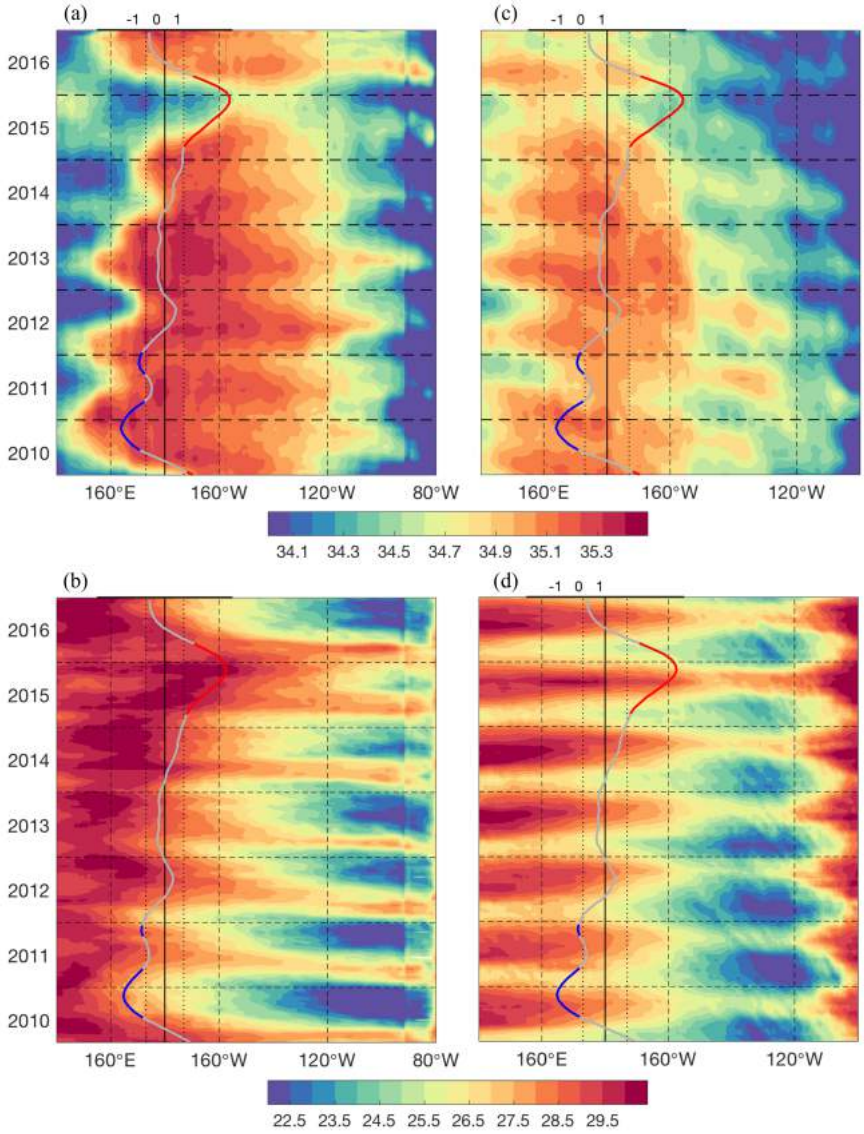

Figure 2. 2010-2016 longitude-time plots of SSS (SMOS) averaged between 2ºS and 2ºN (a) and 16 and 20ºN (c) and of SST (Reynolds) averaged between 2ºS and 2ºN (b) and 18 and 22ºN (d). NINO3.4 on top of all panels, blue during La Niña and red during El Nino.

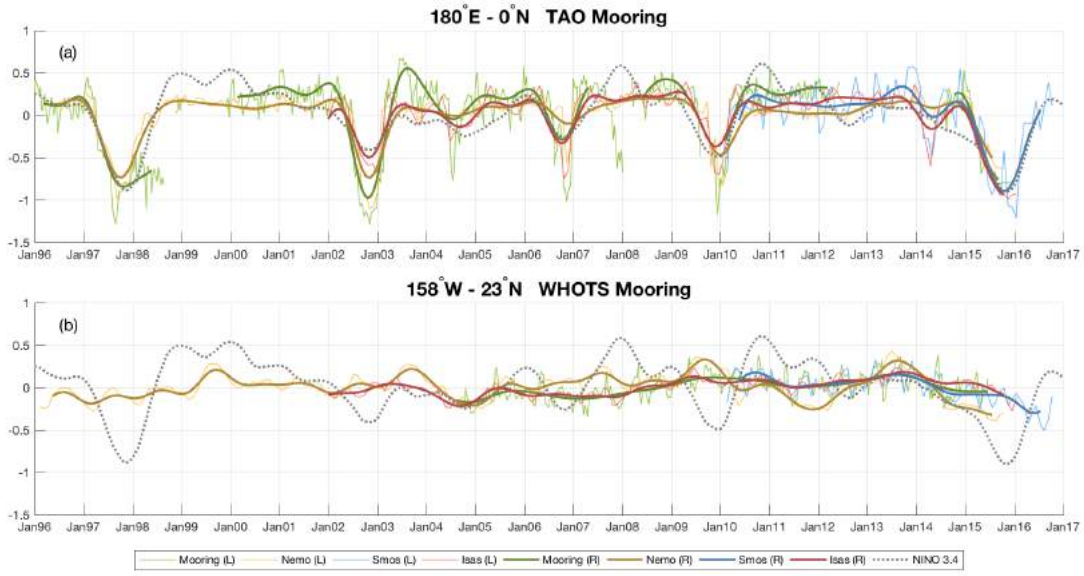

Figure 3. Time series of monthly interannual SSS at (a) the equator and 180ºE and (b) at 158ºW, 23ºN from Moorings (green), ISAS (red), SMOS SSS (yellow) and the NEMO numerical simulation (blue). Lighter colors and thinner lines for the seasonal climatology anomaly (limited filter) and darker thicker lines when using the "robust" filter. The dashed grey line denotes the Niño 3.4 index (-.4 scaling).

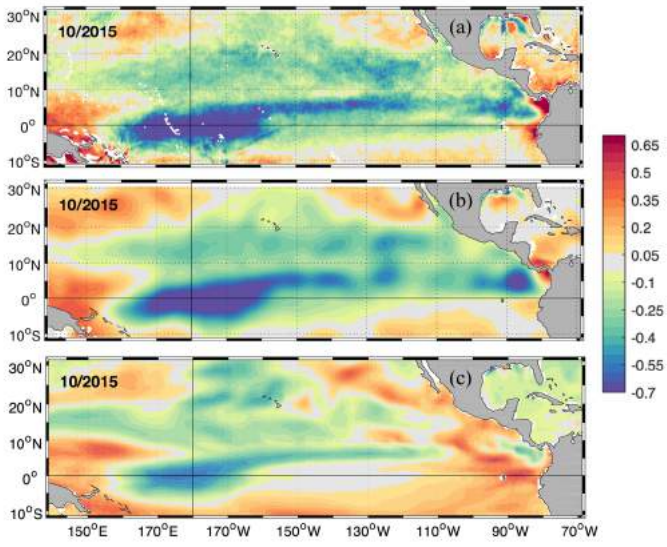

Figure 4. October 2015 SSS Interannual Anomaly from (a) SMOS, (b) ISAS and (c) the model from the "limited" filtering technique.

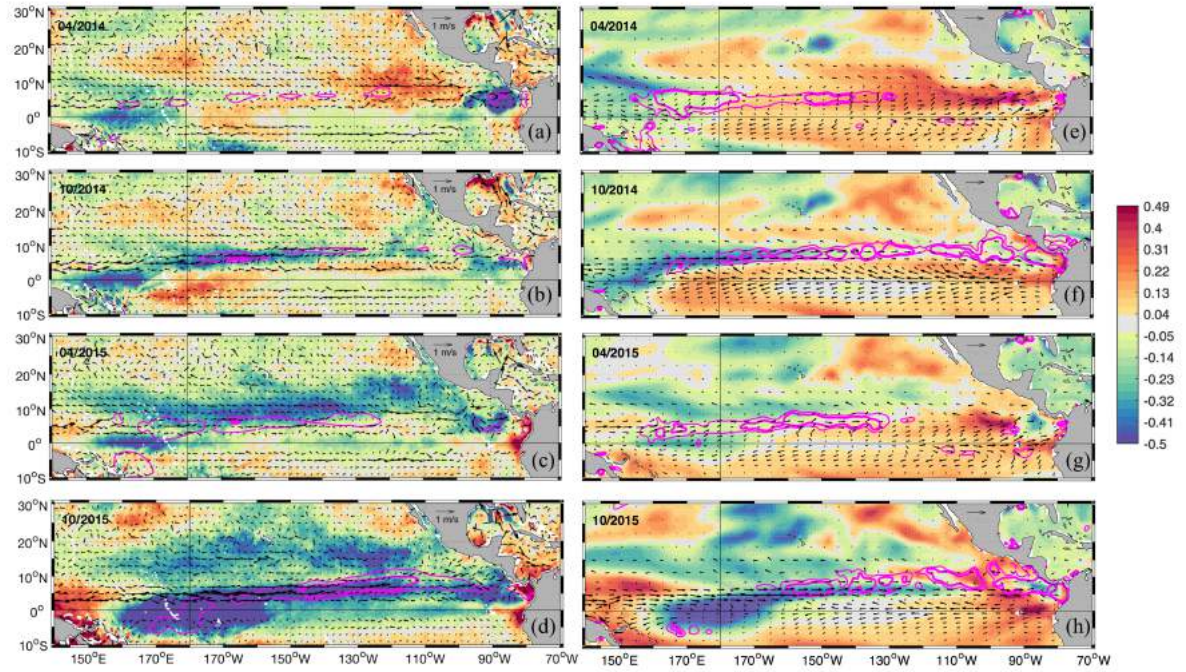

Figure 5. Monthly average, every 6 months, of the interannual SMOS (a-d, left panels) and modelled (e-h, right panels) SSS anomaly (color), unfiltered currents (arrows) and isohyets (-2.5 and -3.5 m.yr-1, magenta contours) for the months of April and October 2014 and 2015.

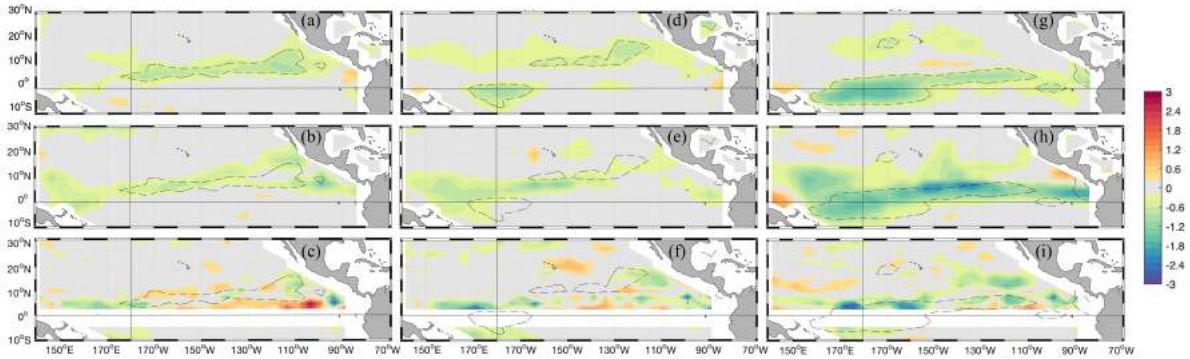

Figure 6. 7-month SSS tendency (a, d, g), fresh water fluxes (b, e, h) and horizontal (c, h, i) advection centered around July 2014 (a-c, left panels), January 2015 (d-f, middle panels) and July 2015 (g-I, right panels) from observations. Panels a, d and g represent SSS changes (Term I of Eq. 2) from April 2014 (Fig. 5a) to October 2014 (Fig. 5b), from October 2014 (Fig. 5b) to April 2015 (Fig. 5c) and from April 2015 (Fig. 5c) to October 2015 (Fig. 5d) respectively. SSS changes associated with freshwater fluxes and horizontal advection (Terms II and III of Eq. 2) over the same

periods are shown on panels b, e, h and c, h, i respectively. Contours on all panels represent the -0.1 year-1 SSS tendency for each period.

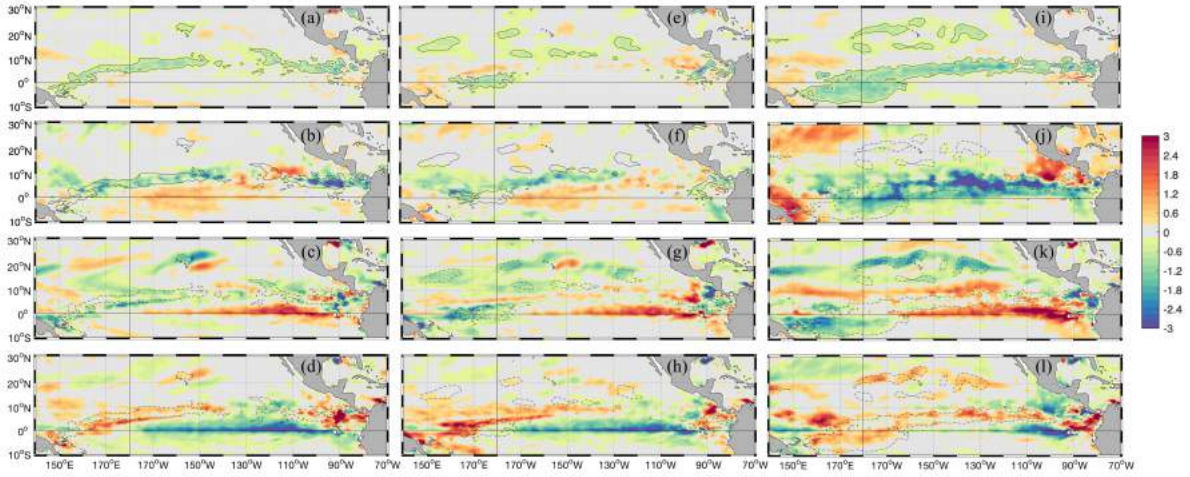

Figure 7. 7-month SSS tendency (a, e, i), fresh water fluxes (b, f, j), horizontal (c, g, k) and vertical (d, h, l) ocean processes centered around July 2014 (a-d, left panels), January 2015 (e-h, middle panels) and July 2015 (i-l, right panels) from the NEMO numerical simulation. Contours on all panels represent the -0.1 year-1 SSS tendency for each period. Analogous to Figure 6.

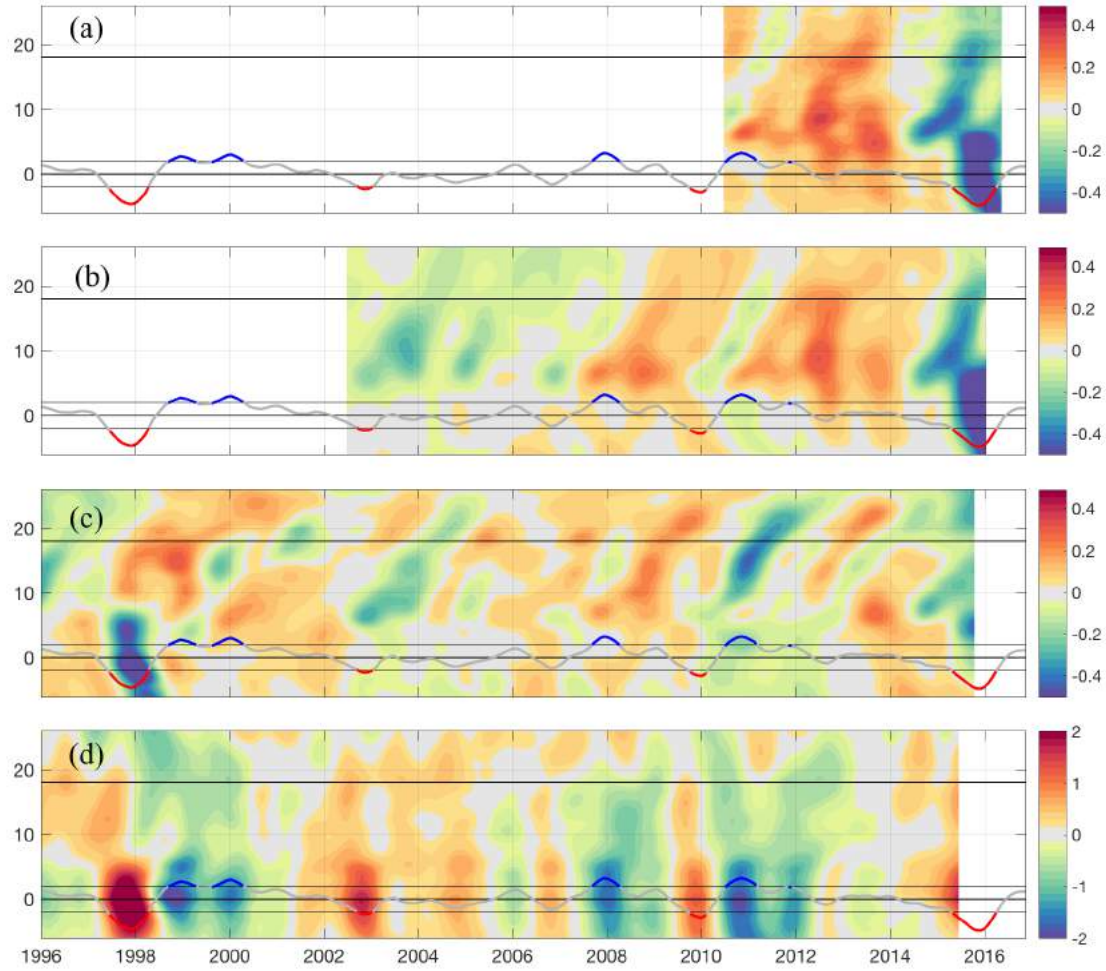

Figure 8. 150º-170ºW Latitude-time plot of the interannual SSS anomaly from (a) SMOS, (b) ISAS, and (c) NEMO and (d) SST from NEMO. NINO3.4 index is superimposed on each panel (blue during La Niña, grey during normal conditions, and red during El Nino events) (scaled by -2, centered on the Equator).

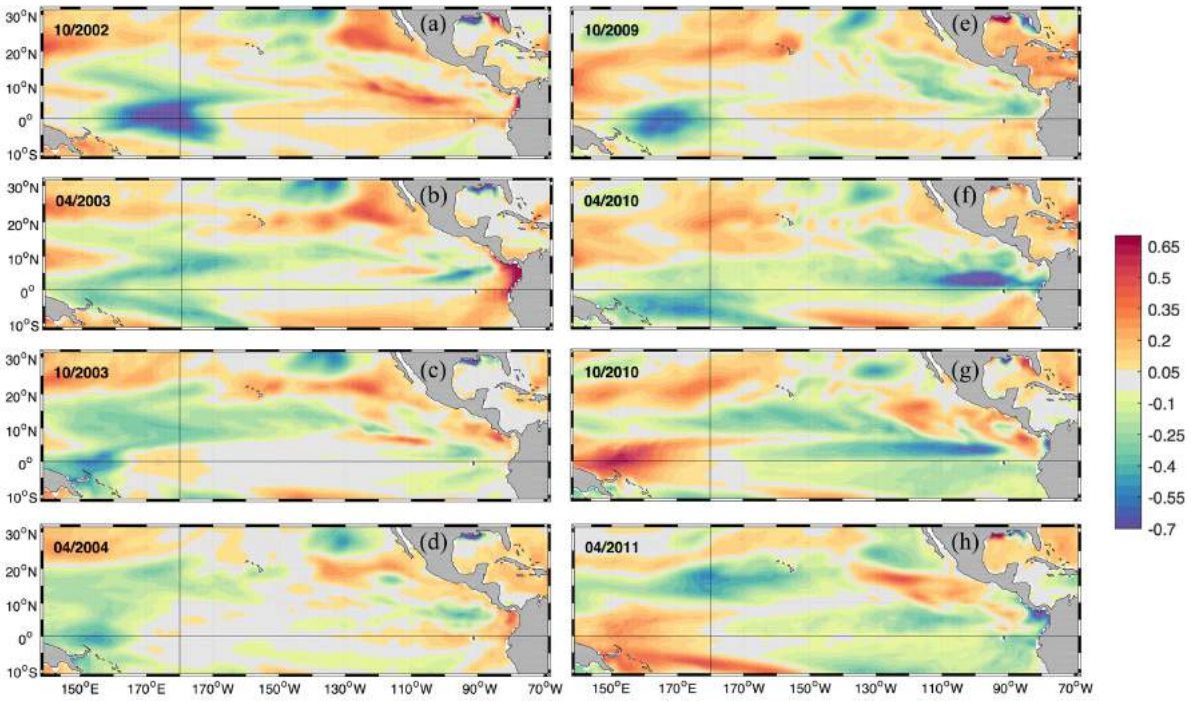

Figure 9. Interannual NEMO SSS anomaly for the months of October 2002 (a), April and October 2003 (b, c), April 2004 (d), October 2009 (e), April and October 2010 (f,g) and April 2011(h).

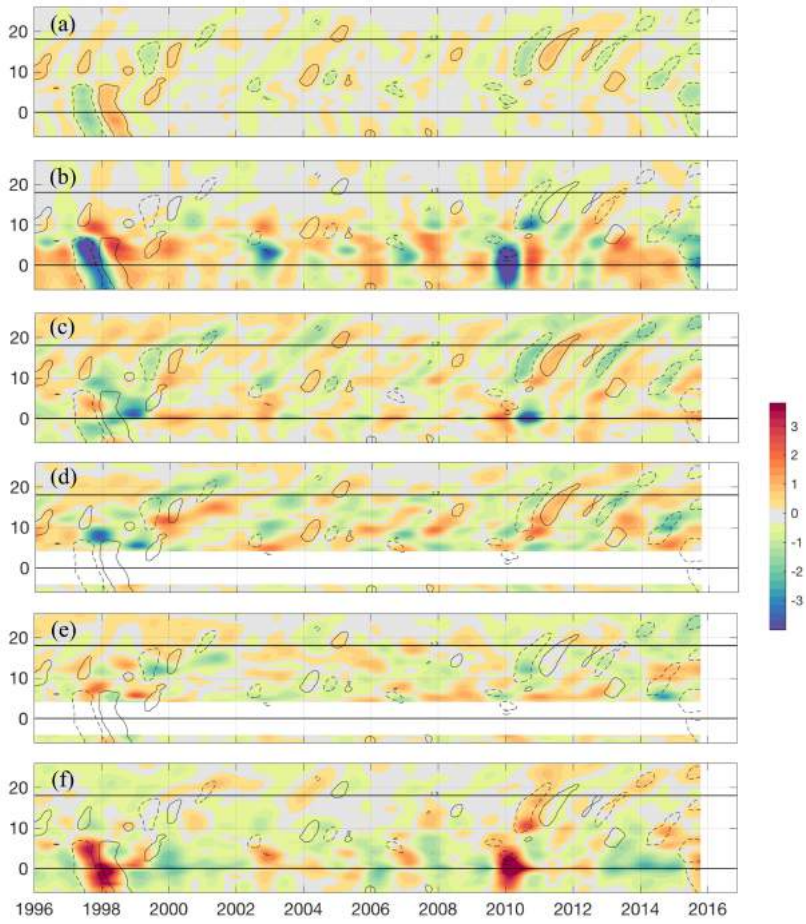

Figure 10. 150º-170ºW latitude-time plots of the interannual NEMO SSS budget as described by Equations 1 and 3: (a) SSS tendency, (b) freshwater fluxes, (c) horizontal processes, (d) Ekman horizontal advection, (e) remaining horizontal processes from the Ekman horizontal advection and (f) vertical processes

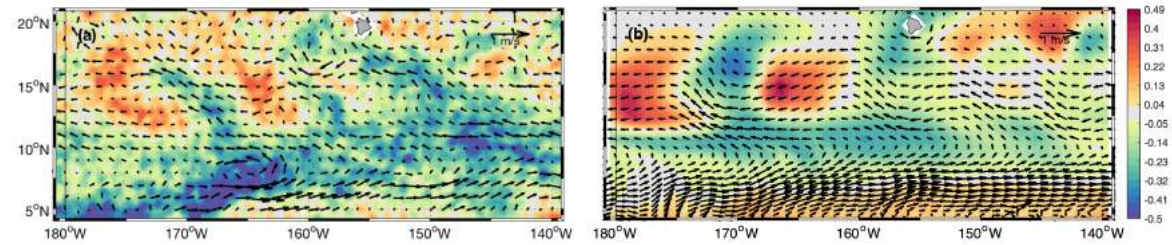

Figure 11. SSSA and currents from (a) SMOS and (b) NEMO for January 2015